

Article

Modeling the Dynamics of Water and Mud Inrush in Fault Fracture Zones: The Role of Seepage–Erosion Interactions

Qingyan Zhang^{1,2,3,*} and Xiaowen Zhou³¹ Guangdong Research Institute of Water Resources and Hydropower, Guangzhou 510610, China² Guangdong Technical Research Center of Geotechnical Engineering, Guangzhou 510640, China³ School of Civil Engineering & Transportation, South China University of Technology, Guangzhou 510640, China; xwzhou@scut.edu.cn

* Correspondence: zhangqingyan1990@126.com

Abstract: By using the principles of porous media seepage mechanics and solute transport theories, a seepage–erosion theory model was developed to uncover the dynamics of mud and water inrush in fault rupture zones during the construction of tunnels. This model consists of a mass conservation equation, a flow transformation equation, a porosity evolution equation, and a permeability evolution equation. These components illustrate the interaction between seepage–erosion particle loss and the transformation of seepage flow patterns throughout the mud and water inrush evolution in the fault fracture zone. This model proves to be effective in illustrating the catastrophic process of mud and water inrushes within tunnels located in fault rupture zones. To address the spatial and temporal variations, the implicit difference and Galerkin finite element schemes were utilized, and the Newton–Raphson iteration method was applied to handle the nonlinear attributes of the equations. The theoretical model underwent further development and numerical simulations were performed using COMSOL multi-field coupling software. A comparison with existing indoor water inrush mud model test results validated the effectiveness of our model. The theoretical model was then applied to the Yong Lian tunnel scenario within the fault rupture zone. This computational analysis exposed the sequence of flow pattern transformations and the instability in seepage–erosion evolution within the fault rupture zone, ultimately leading to the emergence of mud and water inrush disasters. The findings of this study offer valuable insights for addressing tunnel engineering challenges related to underwater inrush disasters.

Keywords: fault; water and mud inrush; seepage–erosion coupling; tunnel engineering

Citation: Zhang, Q.; Zhou, X. Modeling the Dynamics of Water and Mud Inrush in Fault Fracture Zones: The Role of Seepage–Erosion Interactions. *Appl. Sci.* **2024**, *14*, 5115. <https://doi.org/10.3390/app14125115>

Academic Editor: Micòl Mastrocicco

Received: 24 March 2024

Revised: 1 June 2024

Accepted: 7 June 2024

Published: 12 June 2024



Copyright: © 2024 by the authors. Licensee MDPI, Basel, Switzerland. This article is an open access article distributed under the terms and conditions of the Creative Commons Attribution (CC BY) license (<https://creativecommons.org/licenses/by/4.0/>).

1. Introduction

With the launch of the “Western Development” strategy and the progress of the “Belt and Road” initiative, China’s tunnel construction has shifted towards the western mountainous areas, characterized by highly complex geological and topographical conditions. Numerous tunnels that are crucial for infrastructure development in sectors such as transportation, hydraulic engineering, hydropower, and underground national defense are currently under construction [1–3]. Due to the complex geological conditions and the limitations of preliminary explorations, it is challenging to identify all potential risks during the early stages of tunnel construction, leading to frequent occurrences of major geological disasters, including mud and water inrushes. Statistics [4] indicate that fault-type accidents constitute 29% of tunnel-related mud and water inrush disasters. These disasters often caused serious casualties and economic losses, indicating a significant challenge for tunnel construction [5–7]. Therefore, it is necessary to investigate the mechanism of water and mud inrush and to propose control methods to overcome this challenge.

Up to the present, numerous researchers have conducted extensive studies on the mechanisms of mud and water inrush disasters through field and laboratory experiments,

theoretical assessments, numerical modeling, and other approaches. Li Shu-cai et al. [8] introduced an innovative expandable water inrush model experimental system for undersea tunnels, which uncovered the evolution rules of multi-physical fields around faults and the surrounding rock during excavation and water bursting. Focusing on the characteristics of typical faults in China's coal mines, Li Wen-ping [9] carried out a water inrush model experiment with high hydraulic head pressure, revealing multiple changes in the flow pattern throughout the seepage–erosion evolution. Zhang Qing-song et al. [10] developed a mud and water inrush model experimental system for tunnels in fault fracture zones, showcasing the variations in adjacent rock seepage pressure, displacement, stress-strain, and effluent characteristic parameters during tunnel excavation and upon fault exposure. Mao Xie-xing et al. [11,12] reported that rock strata around coal faces are generally in a post-failure state or even in a broken state; therefore, the instability and bifurcation of non-Darcy flow in rock may lead to water irruption and coal and gas outbursts in coal mines. Using an independently designed seepage testing assembly for variable masses of fractured rock, Chen Zhanqing et al. [13] examined the nonlinear seepage traits for variable masses of fractured mud–stone. The seepage pattern of the mud–stone specimens changed immensely during the course of seepage. For the theoretical and numerical modeling, Wang and Park [14] developed a flow-stress water inrush model based on the assumption that the permeability variation was mainly caused by rock deformation during water inrush evolution. Font-Capó et al. [15] proposed a numerical groundwater flow model to predict the location and magnitude of tunnel water inflows in a Barcelona subway. Zhang et al. [16] and Stéphane B. and Maro D. [17] developed different numerical models to simulate the water inrush process from a mechanical perspective. These studies have provided a comprehensive theoretical understanding and practical insights, effectively guiding the forecasting and prevention of such disasters in underground constructions.

However, these methods fall short when dealing with weathered rock, especially fully weathered rock in fault fracture zones, due to its soil-like behavior. The presence of substantial fine particles and minimal cementation in fully weathered rock makes it prone to water erosion and disintegration. The evolution of such disasters in fault fracture zones is thus influenced by both erosion and seepage. On one hand, erosion of the fine particles caused by water flow leads to an increase in porosity and permeability, as reported by many studies [18–20]. On the other hand, the water flow characteristic could be changed from linear Darcy flow to a nonlinear flow state due to the continuous loss of fine particles [21–24]. Given that the flow in the fracture zone is nonlinear, using linear Darcy flow for simulation is impractical. Furthermore, the continuous increase in fracture zone porosity and permeability due to ongoing fine particle loss makes simulating the inrush process with constant porosity and permeability inadequate, as it fails to capture the essence of flow pattern transformation. Therefore, it is crucial to develop an appropriate model for fully weathered fault fracture zones that considers flow–erosion coupling behavior. So far, the erosion behavior has achieved some attention in piping and sand production [25–27]. For example, Sterpi (2003) established a fine particle erosion model by using an empirical relationship between the eroded particle mass and the hydraulic gradient. Papamichos and Vardoulakis (2005) developed an erosion model for sand production with a porosity diffusion law by assuming that the eroded particle discharge follows a gradient law. These studies improved the understanding of erosion behavior and provided important references for erosion-induced water and mud inrush disasters in fault zones. However, more improvement should be made because the water inflow is different from the sand production and piping due to the different stress and flow conditions (e.g., nonlinear flow behavior and high water pressure in tunnel water inrush).

Addressing the gaps in previous studies that overlooked the impact of fine particle erosion on the evolution of fracture zone seepage, this paper introduces a seepage erosion theoretical model that uses solute transport and seepage mechanics theories, establishing a comprehensive theory for mud and water inrush evolution in fault seepage–erosion, including seepage equations and porosity evolution laws. Space and time were discretized

using the implicit difference and Galerkin finite element schemes, while the Newton–Raphson iteration method was used to address the nonlinear characteristics of the equation. The theoretical model was subsequently developed, and numerical simulations were carried out with COMSOL multifield coupling software. Then, this model was applied to a representative case of mud and water inrush in tunnel fault fracture zones, revealing the evolution of such inrush disasters in the fault fracture zones.

2. Theoretical Modeling of Water and Mud Inrush for Completely Weathered Rock in a Fault Fracture Zone

Water and mud inflow in completely weathered rock is a seepage–erosion coupling process, as observed in many experimental investigations [6] (Liu et al. 2018). For example, the flow behavior (e.g., permeability and water flow velocity) is affected by the eroded mass, and the erosion process is controlled by the water flow velocity. Thus, a coupling seepage–erosion water inrush model was developed based on the following assumptions [6] (Liu et al. 2018). (1) The completely weathered rock in fault fracture zones is regarded as a tri-phase system comprising solid grains (s), fluid (f), and fluidized solids (fs), as shown in Figure 1. (2) The fluidized grains are found to be a special solute flowing with the fluid. The interstitial spaces are fully filled with fluidized grains and fluid. (3) The fluidized grain velocity is usually equivalent to the fluid velocity. (4) The fluid is impenetrable, while the solid grains are rigid.

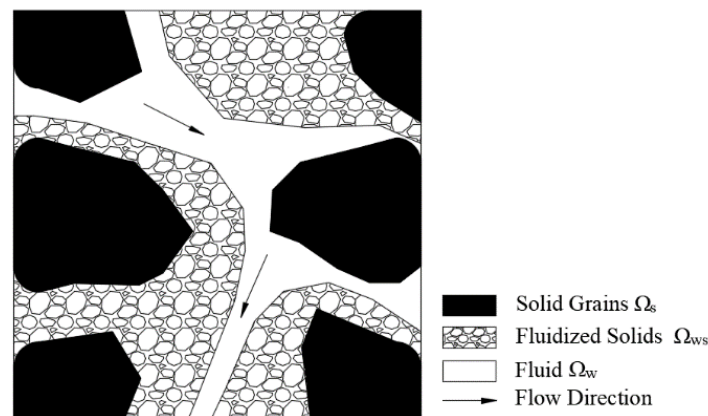


Figure 1. Representative elementary volume.

The governing equations for this coupling water and mud inrush model include a set of mass balance equations for describing the interaction of the different phases (e.g., mass change), a coupled seepage equation for the water flow, a porosity evolution equation for the description of the porosity change caused by the erosion of the fluidized grains, and a permeability evolution equation for the description of the permeability change due to porosity change. These governing equations are illustrated in the following section.

2.1. Mass Balance Equation

The mass balance equation for a multiphase flow system is formulated as shown below [28].

$$\frac{\partial \rho_a}{\partial t} + \text{div}(\rho_a v_a) = \dot{m}_a \quad (1)$$

where the refers to the a phase (e.g., solid grain s (kg), fluidized grain fg (kg), or fluid phase f (kg)), ρ_a (kgm^{-3}) is the partial density (dry density), v_a (ms^{-1}) denotes the real velocity for the phase, and the term \dot{m}_a ($\text{kgm}^{-3}\text{s}^{-1}$) on the right signifies the rate of mass generation. In this equation, the first term on the left signifies the rate of partial density change, and the second term is the net accumulation term for the phase.

Based on the Dupuit–Forchheimer law (J. Bear 1972) [28], the volume discharge \bar{v}_i (ms^{-1}) for a fluid–particle mixture is related to the seepage velocity \bar{q}_i (ms^{-1}), as shown below.

$$v = q/\varphi \quad (2)$$

Hence, the mass balance equations for the three phases are formulated.

Solid grain phase:

$$\frac{\partial \varphi}{\partial t} = \frac{\dot{m}_s}{\rho_s} \quad (3)$$

Fluidized grain phase:

$$\frac{\partial(c\varphi)}{\partial t} + \frac{\partial(c\bar{q}_i)}{\partial x_i} = \frac{\dot{m}}{\rho_s} \quad (4)$$

Fluid phase:

$$\frac{\partial \bar{q}_i}{\partial x_i} = 0 \quad (5)$$

where ρ_s (kgm^{-3}) is the real density of the soil particle (i.e., particle density), φ is the porosity of the porous medium (the ratio between the void volume and the total volume), and c is the concentration of the fluidized grain in the fluid–particle mixture (the ratio between the fluidized grain volume and the void volume).

2.2. Flow Pattern Evolution Equation

Through the indoor model test and previous extensive field engineering experiences [29,30], it was determined that the evolutionary process of water bursting in the fully weathered rock within the fault fracture zone can be divided into the following three phases: (1) The initial linear flow phase, during which the fluid initially flows at a considerably slow rate, exhibiting a linear laminar pattern. (2) The nonlinear seepage phase, during which an increase in porosity occurs due to the loss of particles, leading to a rapid increase in flow velocity. There is a transformation of seepage from linear Darcy flow to nonlinear flow in the fault fracture zone, which is a key stage of fault mud and water inrush evolution. (3) The pipe flow phase, which occurs after the establishment of a water inrush channel where the flow is converted into pipe flow.

To distinguish the flow pattern transformation during water burst evolution in the fully weathered rock in the fault rupture zone, Re is adopted in this study. According to the relationship between the friction coefficient and Re [31], when $Re < 5$, the flow belongs to the initial linear phase. When $5 < Re < 200$, it belongs to the nonlinear seepage stage, and when $Re > 200$, it belongs to the pipe flow stage.

When $Re < 5$, the water flow pattern enters a linear laminar stage, and Darcy's law is applicable to low-permeability porous media in the initial linear flow phase of water bursts. The following form of Darcy's law is taken (J. Bear 1972) [28].

$$\bar{q}_i = -\frac{k}{\eta_\kappa \bar{\rho}} (\nabla p + \bar{\rho} g Z) \quad (6)$$

where p (Pa), g (mS^{-2}) and Z (m) denote the pore pressure, acceleration of gravity and height, respectively; η_κ (m^2S^{-1}) signifies the kinematic viscosity of the fluid; $\bar{\rho}$ (kgm^{-3}) represents the real density of the fluidized grain–fluid mixture, $\bar{\rho} = (1-c)\bar{\rho}_f + c\bar{\rho}_s$; and k signifies the intrinsic permeability of the porous medium.

In the case where $5 < Re < 2000$, the water flow pattern is a nonlinear seepage stage, and Brinkman's equation is probably more applicable to the flow characterization of high-speed fluid in a highly porous medium while considering the shear stress of viscous fluid

in high-speed fluid. The relevant equation is formulated as shown below (Brinkman 1949) [32]:

$$\left. \begin{aligned} (\eta_k/k)q_i &= \nabla \left[-pI + \eta_k \left(\nabla q_i + (\nabla q_i)^T \right) \right] + F \\ \nabla q_i &= 0 \end{aligned} \right\} \tag{7}$$

In the case where $Re > 2000$, the water flow pattern is a pipe flow stage, for which the Navier–Stokes equation is appropriate. The following equation is used.

$$\left. \begin{aligned} \bar{\rho}q_i \nabla q_i &= \\ \nabla \left[-pI + \eta_k \left(\nabla q_i + (\nabla q_i)^T \right) \right] + F \\ \nabla q_i &= 0 \end{aligned} \right\} \tag{8}$$

On the basis of the preceding analysis, we develop a coupled Darcy–Brinkman–Navier–Stokes equation to depict the flow pattern changes during the evolution of water inrush in the completely weathered rock of the fault fracture zone. For porous media, the coupled equation in the completely weathered rock of the fracture zone can be expressed as follows:

$$\left. \begin{aligned} \frac{\bar{\rho}}{\varphi} \left(q_i \nabla \frac{q_i}{\varphi} \right) &= \nabla(-pI) + \\ \nabla \left\{ \frac{1}{\varphi} \left[\eta_k \left(\nabla q_i + (\nabla q_i)^T \right) - \right] \right\} &- \frac{\eta_k}{k} \bar{q}_i + F \\ \nabla q_i &= 0 \end{aligned} \right\} \tag{9}$$

The left side of Equation (9) represents the inertia term of the Navier–Stokes equation. The second and third terms on the right side correspond to the viscous terms of Brinkman’s model and Darcy’s law, respectively. As indicated by Equation (7), simplification of Darcy’s equation is feasible by neglecting both the inertia term and the viscous term of Brinkman’s model when the flow velocity is extremely low. As the system evolves into a non-linear seepage phase, this simplification becomes advantageous if the viscous term of Brinkman’s model plays a significant role. Once the channel is established, there is an increase in the Navier–Stokes inertia term, leading to an approximation of the equation to Equation (8) to describe the third phase.

2.3. Porosity Evolution Law

To address erosion or mass transfer problems in porous media, a fine particle migration equation is developed to describe the porosity evolution law based on the erosion process of piping and sand production [33,34].

$$\frac{\partial \varphi}{\partial t} = \lambda(1 - \varphi)c|q| \tag{10}$$

where λ (m^{-1}) stands for the coefficient of the porosity evolution equation, and $|q|$ represents the absolute value of the volume discharge, q .

2.4. Permeability Evolution Law

The Kozeny–Carman [35] formula can effectively express the permeability k in a porous medium with a high initial permeability,

$$k = k_0 \left(\frac{\varphi}{\varphi_0} \right)^3 \left(\frac{1 - \varphi_0}{1 - \varphi} \right)^2 \tag{11}$$

where k_0 and φ_0 are the initial permeability and initial porosity of the porous media, respectively.

In summary, the enclosed equation sets consist of Equations (3)–(5) and (9)–(11), which can be used to solve the process variables p , φ , c , and k . In particular, these partial differential equations are solved by importing them into the COMSOL multiphysics system,

with the utilization of implicit difference and Galerkin finite schemes to discretize time and space. Furthermore, the Newtown–Raphson iteration is applicable for deriving the solution considering the nonlinearity of the equation set.

3. Validation of the Model

To validate the theoretical model of seepage and erosion in the fault fracture zone, comparisons between the laboratory water and mud inrush tests and numerical results were performed in the following section. Three laboratory tests with water pressures of 0.4, 0.7, and 1.0 MPa were carried out.

3.1. Description of the Experimental Tests

The experimental tests of the erosion-induced water and mud inrush disaster were performed by using a self-designed large-scale triaxial testing system (Figure 2). The experimental system consisted of a pressure control system, a particle transfer permeability testing system, data collection equipment, and water and mud collection equipment. A hollow base pedestal with a hole-based flow piston was designed for particle transfer and water flow.

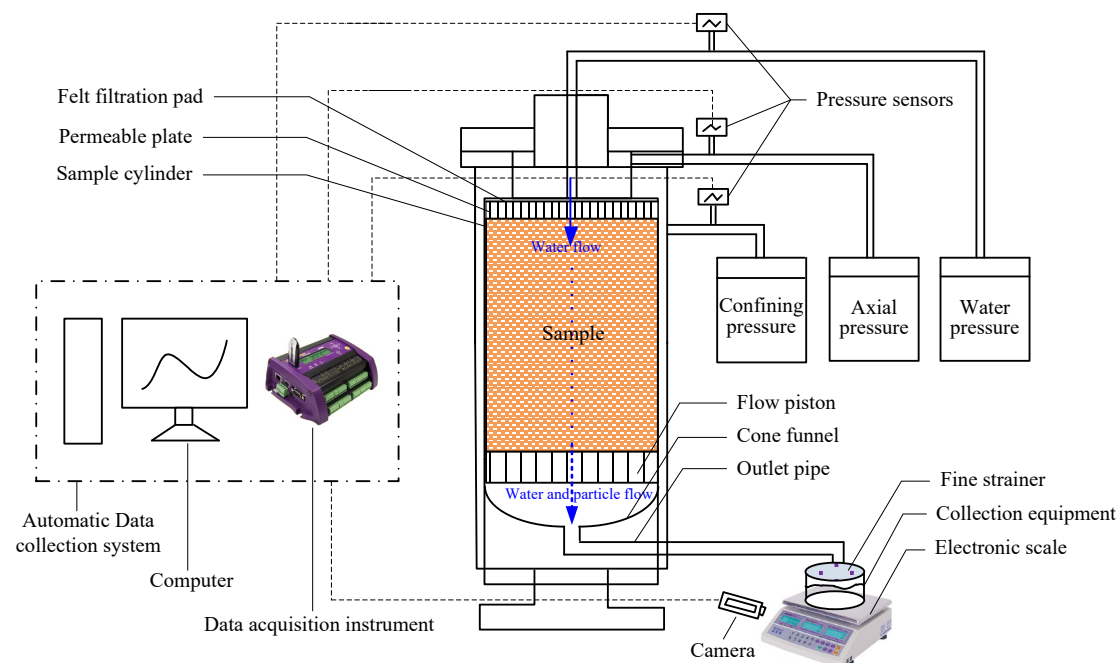


Figure 2. Large-scale triaxial testing system [6,36].

The testing soil was obtained from a fault rupture zone during the construction of tunnels (i.e., Yonglian tunnel in Jiangxi, China) [36] (Zhang et al. 2020). The diameter and height of the sample were 15 cm and 20 cm, respectively. The stress conductions of these tests were determined according to the burial depth of the tunnel (around -100 m), namely the axial pressure of 2 MPa and the confining pressure of 1 MPa. Different water pressures were considered to investigate their influence on the evolution of water and mud inrush. The basic procedure for these tests included: (i) sample installation and saturation; (ii) application of the axial and confining loads; and (iii) application of the water pressure and data collection. The criteria for the test termination is that no particles are eroded.

Three tests with different water pressure were conducted in this study, namely, 0.4, 0.7, and 1.0 MPa. Through these tests, the transient seepage–erosion behavior can be obtained, e.g., porosity, permeability, and water and mud inflow. More details of these experiments (e.g., experimental device and procedure, soil properties, parameter measurement) can be found in the previous studies [6,36].

3.2. Numerical Simulations

According to the laboratory tests, a numerical model with the same size was established, as shown in Figure 3. Table 1 presents the initial conditions and boundary conditions of the numerical model. The initial water pressure in the domain was determined from an initial steady analysis. A water pressure boundary condition was applied to the upper boundary of the model. The value of the water pressure followed the experimental tests (i.e., 0.4, 0.7, and 1.0 MPa) [36]. An outlet water boundary measuring 1 cm in length was established at the bottom, and the four boundaries of the model were made impermeable. The left and right boundaries were impervious boundaries. The fluidized grain concentration in the upper boundary was 0.01. A free boundary of the fluidized grain concentration was set at the exit of the bottom, allowing for the free movement of the particles with water. The other boundaries of the fluidized grain concentration were insulation boundaries. In the simulation, the computation was conducted for 1500 s.

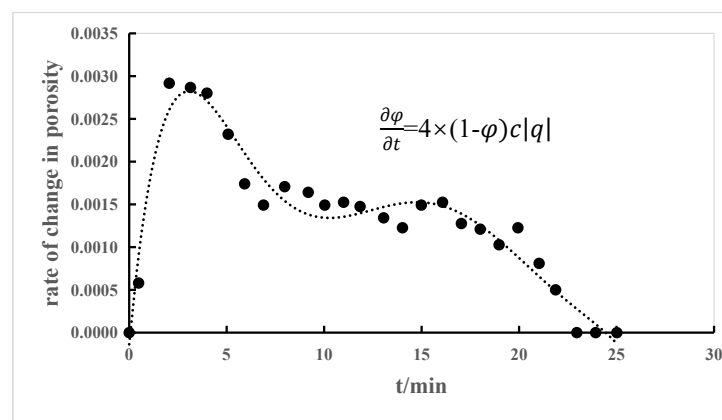


Figure 3. Large-scale triaxial testing system [6,36].

Table 1. Physical parameters of the numerical verification model.

Initial porosity φ_0	0.35
Initial fluidized grain concentration c_0	0.01
Pore pressure on the outer boundary p_d /MPa	0
Upper-pressure boundary p_u /MPa	1.0/0.7/0.4
Coefficient λ /m ⁻¹	4
Real density of fluid ρ^w /kgm ⁻³	1000
Real density of grains ρ^s /kgm ⁻³	2650
Kinematic viscosity of fluid η_k /m ² s ⁻¹	1×10^{-6}
Initial permeability k_0 /m ²	5×10^{-12}
Initial porosity φ_0	0.35

3.3. Calibration of Parameters

The physical properties of the tested soils are summarized in Table 1. The initial porosity before the water and mud inrush test is 0.35. The real density of the soil particle is 2650 kg/m³ using the pycnometer method and the initial permeability is 5×10^{-12} m² using the permeability test. The erosion coefficient λ in the porosity evolution law is calibrated by fitting the time evolution of the porosity change rate in the erosion-induced water and mud inrush tests of 0.4 MPa. As shown in Figure 3, the λ can be determined as 4. All these parameters are provided in Table 1.

3.4. Comparisons between Model Prediction and Laboratory Experiments

Figure 4 illustrates the numerical model, which has a diameter of 0.15 m, a height of 0.3 m, and an outlet boundary width of 0.01 m. Figures 5 and 6 display the comparison of evolution curves for water flow rate and particle loss between the numerical simulations

and experiments, with water pressures fixed at 0.4, 0.7, and 1.0 MPa. The comparison results are illustrated as follows:

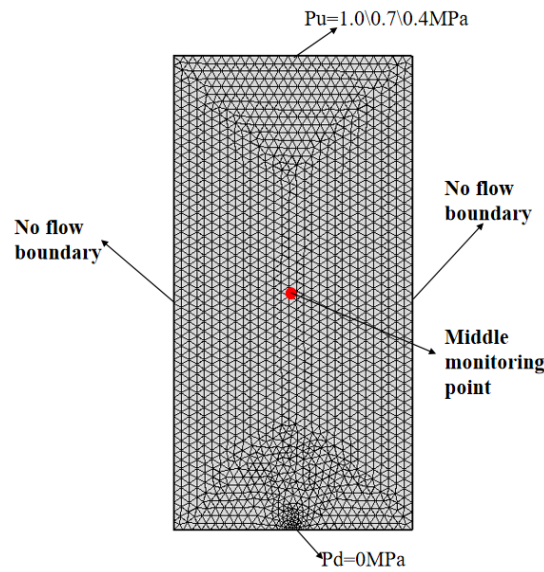


Figure 4. Numerical verification model.

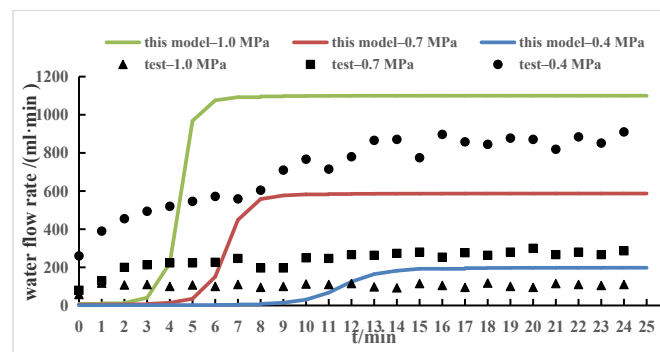


Figure 5. Time variation of the water flow rate.

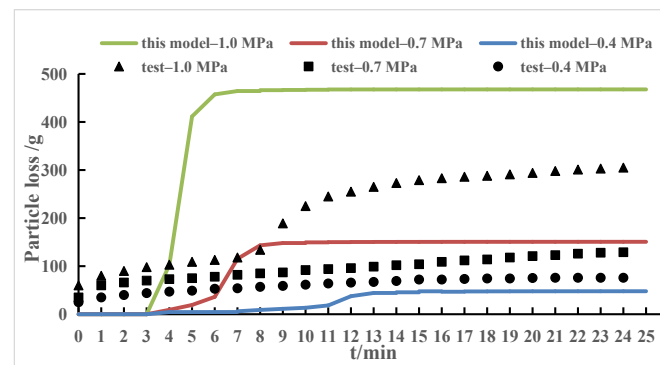


Figure 6. Time variation of the particle loss.

Figure 5 provides the comparison results of water inflow rate under different water pressures. It can be observed that the numerical model simulations are consistent with the laboratory model experiment data, which generally have a similar variation trend. In particular, the nonlinear increase of the water flow after a certain time can be reflected in the numerical simulation, e.g., the water flow changes from a Darcy linear flow to rapid

flow after 5 min when $p = 1.0$ MPa. This result demonstrates that the proposed model is able to reproduce the nonlinear flow of the water inrush. Furthermore, the magnitude of the predicted values is also comparable. For example, the final water inflow rate from the numerical study for $p = 0.4$ MPa was 145 mL/min, which is similar to the test result of 110 mL/min.

For the eroded mass of the particles (see Figure 6), similar behavior can be observed compared to the result of the water flow rate. The time variation of the particle losses between the numerical investigations and laboratory tests shows a similar trend. The predicted particle losses are generally accepted for different water pressures. For example, when $p = 0.4$ MPa, the final particle loss is about 50 g in the numerical simulation, being 85% of the result in a laboratory test. Comparison from the above results suggests that the proposed model can well predict the evolution of the water–mud inflow in the completely weathered granite in the fault zone.

However, some differences between numerical investigations and laboratory tests could also be observed, possibly attributed to the modeling method of the outlet in the numerical investigation. An outlet water boundary with 1 cm length was used, which is different from the outlet with the uniform small hole in the flow piston.

4. Engineering Application

4.1. Geometry and Finite Element Model

During the construction at the Yonglian tunnel entrance up to the F2(ZK91 + 325~ZK91 + 325) fault fracture zone in Jiangxi Province of China [37,38], water and mud inrush catastrophe occurred. The F2 fault surface crosses the section ZK91 + 350, trending SSE, intersecting the tunnel axis at a 45° angle, dipping to the east with an angle of 84°, and has a width of 15 to 35 m, predominantly filled with argillaceous materials, and the stratum has a high water content.

Figure 7 depicts the finite element model and geometry of the fault and fractured zones in the Yong Lian tunnel, which measures 400 m in length and 360 m in height. A fault fracture zone (F2:ZK91 + 325~ZK91 + 325) with high water pressure exists in front of the heading face, with a dip angle of 84° and a width of 25 m from the tunnel face. Table 2 outlines the physical parameters based on literature reference [38]. Initial settings include porosity (φ) at 0.3 and fluidized grain concentration (c) at 0.05. Boundary conditions entail pore pressures of 0, 0, and 2 MPa applied separately at the outlet, upper, and bottom boundaries, with the others having no flow boundary. The Dirichlet condition is adopted at the interface of surrounding rock (P1, V1) with fault (P2, V2), ensuring continuous boundary pressure and velocity. After 550 min of initial steady seepage computation, we derive the initial pore pressure for the entire region. Figures 8 and 9 illustrate the temporal fluctuations of porosity, pore pressure, and fluidized grain concentration, respectively. Figures 10–12 demonstrate the development of the water inrush channel.

Table 2. Physical parameters.

Initial porosity φ_0	0.3
Initial fluidized grain concentration c_0	0.05
Pore water pressure on the upper boundary p_d /MPa	0
Pore water pressure on the bottom boundary p_d /MPa	3.6
Coefficient λ of fault/ m^{-1}	4
Coefficient λ of surrounding rock/ m^{-1}	0.01
Real density of grains ρ^s /kgm ⁻³	2650
Fluid viscosity η_k /m ² s ⁻¹	1×10^{-6}
Initial permeability k_0 of fault/m ²	5×10^{-12}
Initial permeability k_0 of surrounding rock/m ²	1×10^{-13}

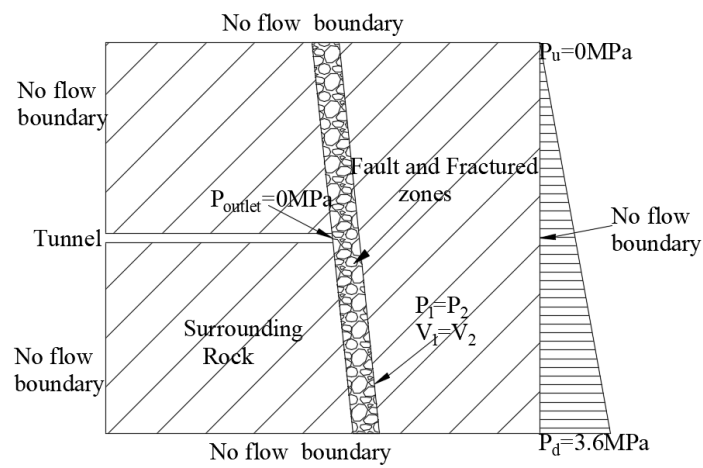


Figure 7. Tunnel water inrush model.

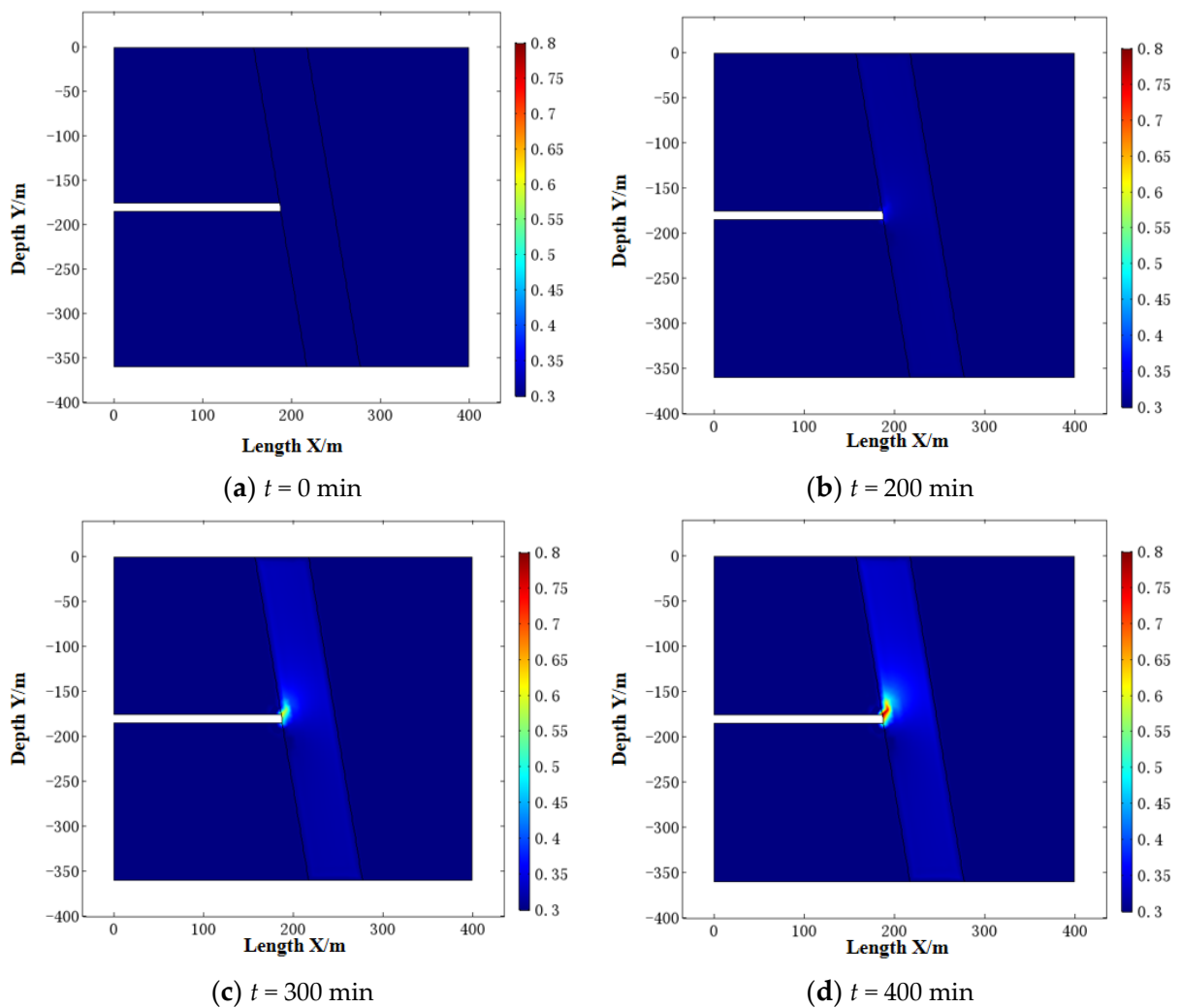


Figure 8. Cont.

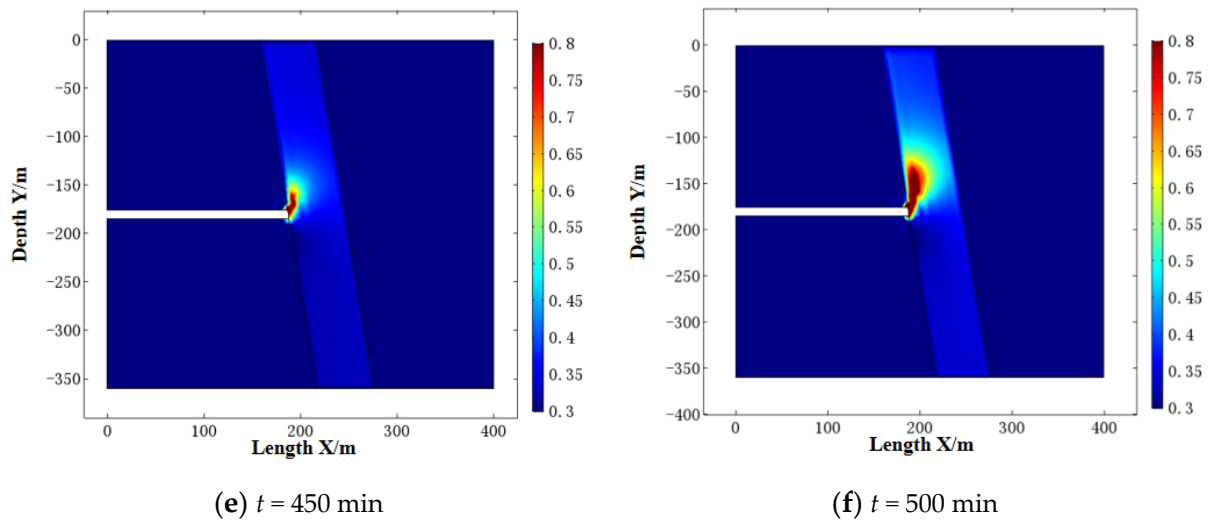


Figure 8. Time variation in the porosity.

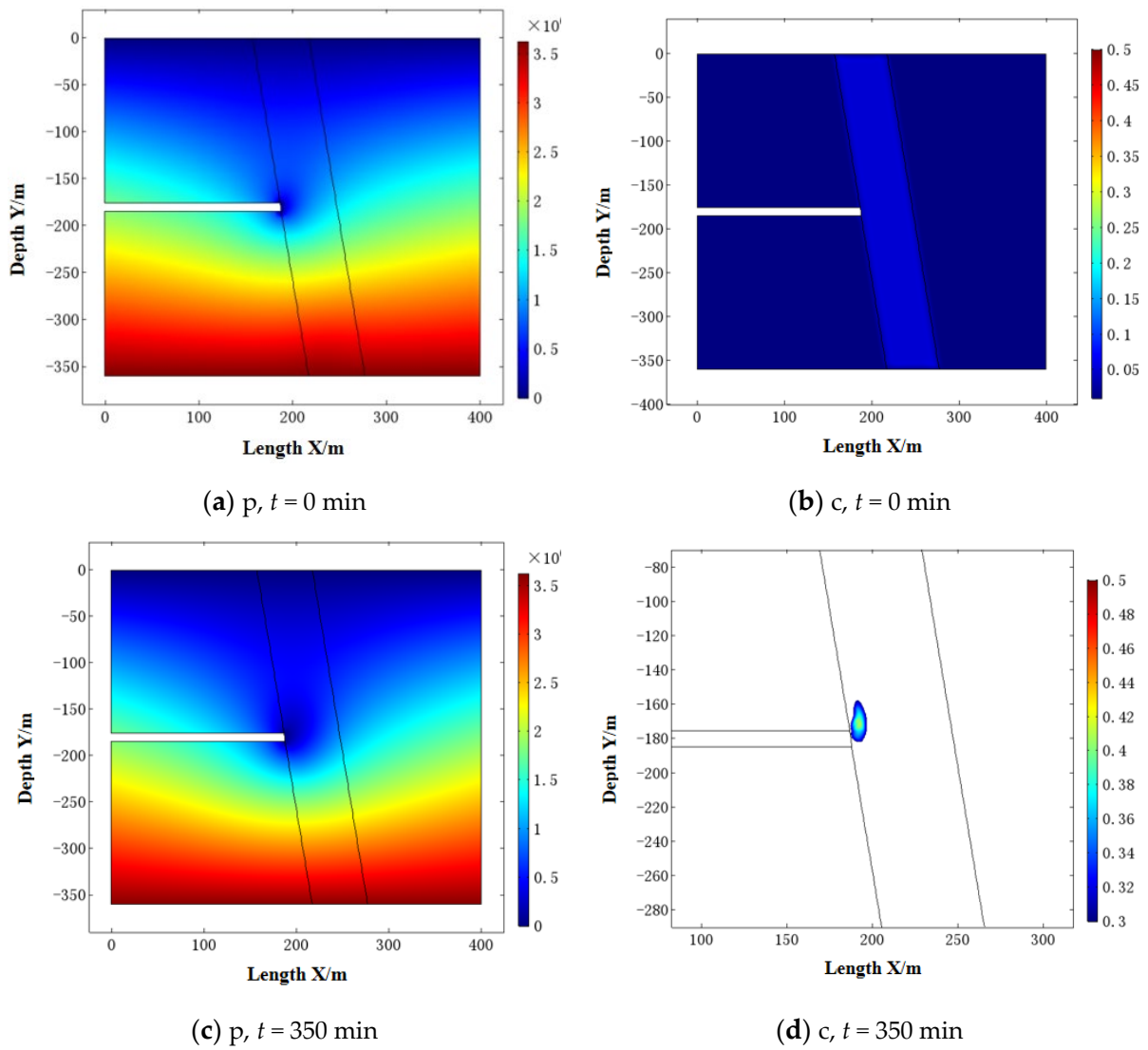


Figure 9. Cont.

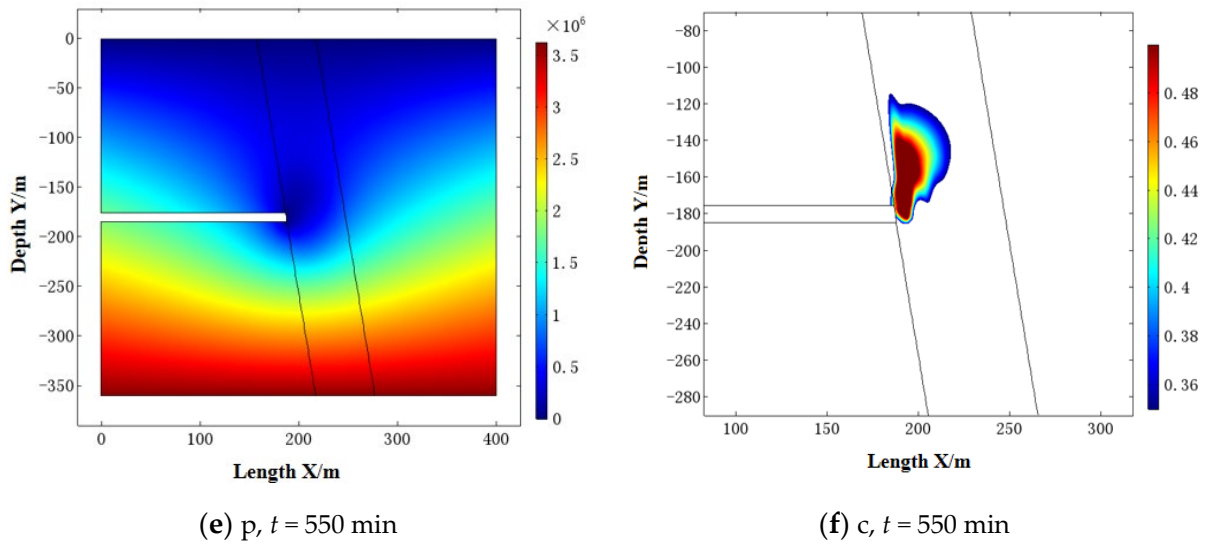


Figure 9. Time variations in the pore water pressure p and fluidized grain concentration c .

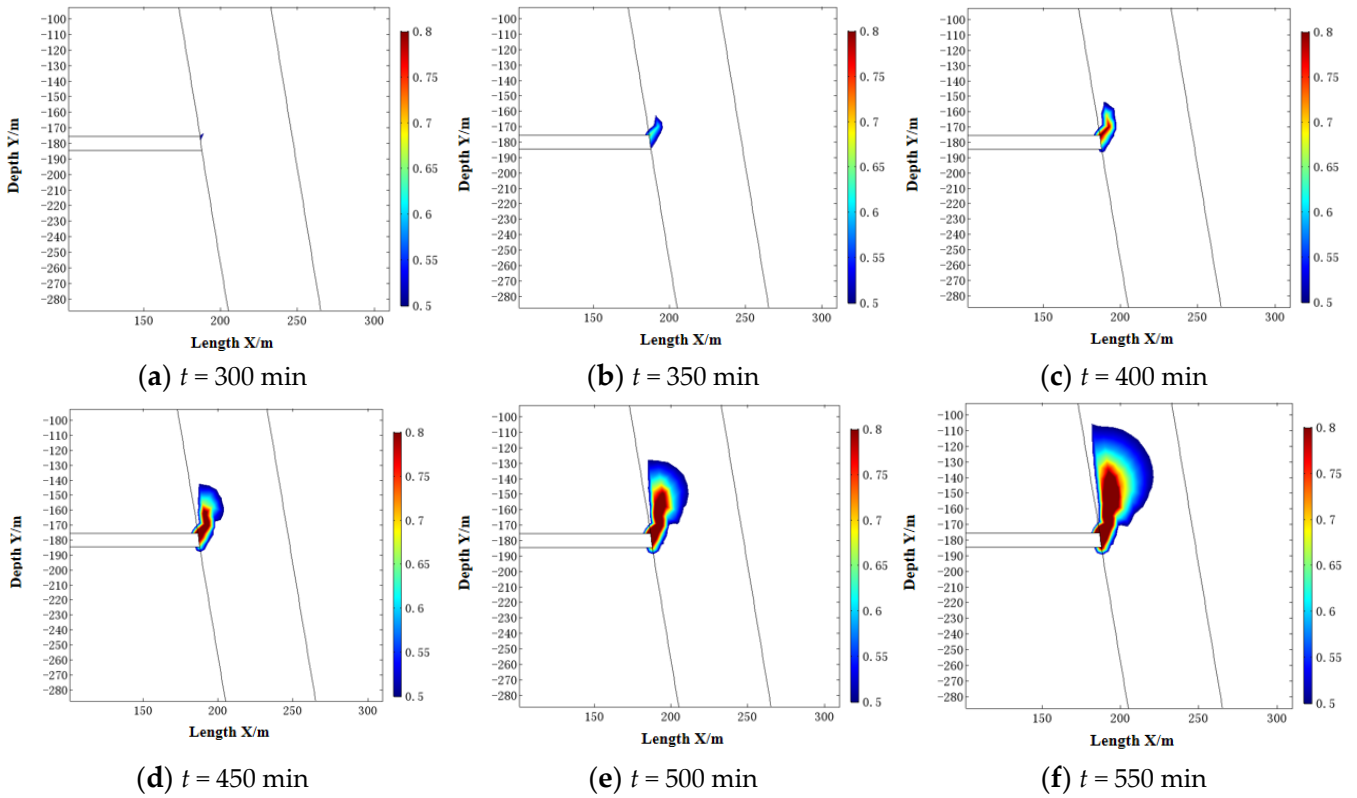


Figure 10. Changes in the porosity over 0.5 in the fault zone over time.

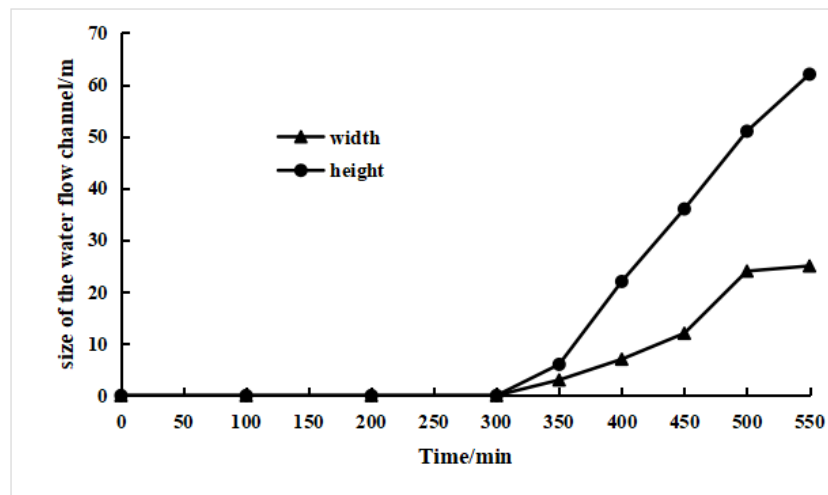


Figure 11. Time variation in the average channel size.

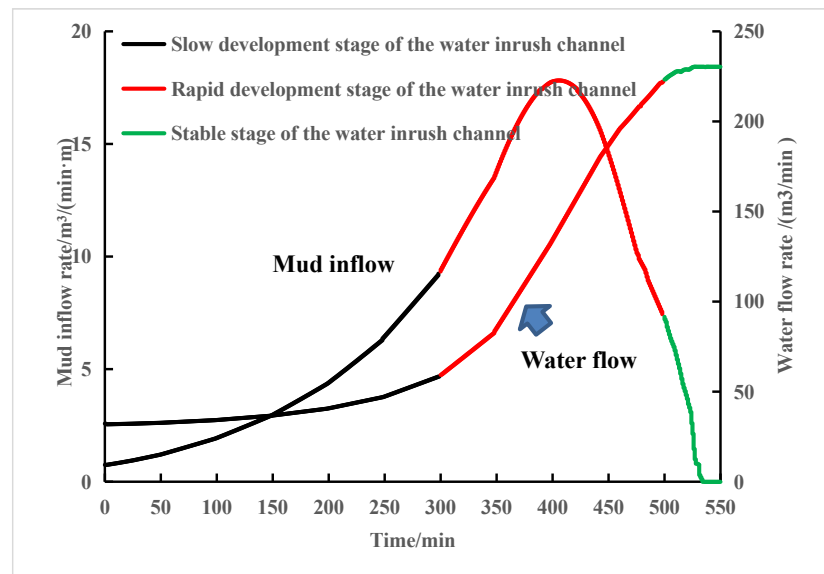


Figure 12. Temporal variation in the water flow rate and mud inflow rate at the outlet boundary of the tunnel face.

4.2. Model Calculation Results and Analysis

(1) Porosity evolution.

Figure 8 shows the results of porosity evolution contours. As depicted in Figure 8, porosity changes are insignificant near the exit and in the fault rupture zone when the evolution time is below 200 min. At 300 min, porosity changes dramatically near the exit zone, with a maximum porosity of approximately 0.55. This indicates more active erosion and considerable particle loss. By 400 min, the maximum porosity near the exit zone reaches close to 0.8, with drastic alterations in the fault fracture zone vicinity, suggesting considerable particle loss and unstable cavity formation. With continued evolution, porosity development increases between the exit and fault fracture zone, with regions exceeding 0.8 porosity transfixing rapidly, indicating the formation of the water inrush channel.

(2) Pore water pressure and fluidized grain concentration evolution.

Figure 9 shows the results of the pore water pressure and fluidized grain concentration at different times. When the evolution time is 350 min, more active erosion is observed near the exit zone. The maximum fluidized grain concentration at the exit zone is close to 0.35,

the pore pressure around the model outlet decreases gradually with increasing evolution time, and the pore pressure gradually forms a low-pressure funnel area at the model outlet, which grows larger with increasing evolution time, as shown in Figure 9b,c. With significant particle loss, unstable cavities formed in the fault fracture zone. As the evolution progresses, the porosity between the exit and fault fracture zones quickly increases to 0.5 (Figure 9e). This indicates that all the movable particles have been eroded except for the large skeleton particles, and a water inrush channel has formed (see Figure 9f).

- (3) Analysis of the development of the water inrush channel and the water and mud inrush disaster.

Soil with high porosity will induce the collapse and result in the formation of the water flow channel. To analyze the development of the water inrush channel, the zone with high porosity (>0.5) was further investigated, as shown in Figure 10. It can be observed that a porosity greater than 0.5 first appeared in the tunnel vault at $t = 300$ min, which inclined to the tunnel axis at an angle of approximately 45° . As the evolution continued, the porosity development increased in the fault fracture zone (Figure 10b–d), and the region with a porosity exceeding 0.5 rapidly developed toward the fracture zone top, as depicted in Figure 10e,f, suggesting the establishment of a water inrush channel. Channel formation further exacerbates erosion development because of the elevated fluidized grain concentration and flow velocity. As depicted in Figure 10e,f, the channel width and height increase with continual erosion.

To quantitatively evaluate the size of the water inrush channel, the porosity of the water inrush channel or cavity was set to greater than 0.7. Based on this criterion, the temporal evolution of the mean water inrush channel size was determined in Figure 11. From 0 to 350 min, the channel height and width are considerably small owing to the weak erosion, which is approximately zero. From 350 to 500 min, the water inrush channel develops rapidly, and the channel height increases quickly from 0 to approximately 50 m. The width of the channel increases rapidly from zero to approximately 25 m. After channel formation, its width remains stable, while its height increases quickly from 50 m to 62 m.

Figure 12 illustrates the temporal fluctuations of the water flow rate and mud inflow rate at the outlet boundary of the tunnel face. Combining this analysis with Figure 11, we segment the development process of the water outburst channel into three phases: slow development, rapid development, and stable phases. During the slow development phase, the water flow rate and mud inflow rate increase gradually. In the rapid development phase, both rates increase rapidly, with mud inflow reaching a maximum above $17.8 \text{ m}^3/(\text{min}\cdot\text{m})$ before decreasing rapidly. In the stable phase, the water flow rate remains above $230 \text{ m}^3/\text{min}$, while the mud inflow rate decreases rapidly to zero.

During water outburst channel development, mud inflow resulting from seepage erosion is significant, as evidenced by the seepage–erosion water inrush model. Consequently, this developed model offers significant advantages in forecasting water inrush channel development in fault fracture zones during tunnel construction.

5. Conclusions

Based on the theories of the porous media seepage mechanics and solute transport, a seepage–erosion coupling model was developed to describe the complex water and mud inrush evolution process during tunnel construction in a fault zone and its effectiveness was verified with laboratory tests. In this model, the erosion behavior (i.e., fine particle loss caused by seepage) was modeled by using a porosity evolution equation. The hydraulic behavior was described by using a coupling Darcy–Brinkman–Navier–Stokes equation, which can effectively describe the flow pattern change during the evolution process of water and mud inrush and significantly improves the prediction performance compared to the traditional model, with only considering a linear flow. By using this model, the dynamic variations in particle loss, pore pressure, permeability, porosity, and water inflow caused by particle mass transfer can be obtained and the whole evolution process of water

and mud inrush can be modeled, which overcomes the deficiencies in existing water inrush mechanism modeling.

Furthermore, under complex boundary and flow conditions, this model was used to simulate the water inrush development and achieved good results in predicting the direction, channel size, and whole evolution process of water and mud inrush in fault rupture zones during the construction of tunnels. These improvements make up for the shortage of existing research on water inrush mechanism modeling and provide a new method for the design of prevention measures for water inrush, such as curtain grouting technology. The research findings from this paper can benefit tunnel engineering in the case of water inrush disasters.

However, due to the ignorance of the mechanical behavior, the large deformation and the collapse of the surrounding rock at the post-disaster water and mud inrush cannot be well captured. Furthermore, this model cannot be used in fractured rock masses within fault fracture zones because water and mud inrush in these zones are primarily controlled by the fracture change instead of the seepage–erosion effect.

Author Contributions: Conceptualization, Q.Z. and X.Z.; methodology, Q.Z. and X.Z.; software, Q.Z.; validation, Q.Z.; formal analysis, Q.Z.; investigation, Q.Z. and X.Z.; resources, Q.Z. and X.Z.; data curation, Q.Z.; writing—original draft preparation, Q.Z.; writing—review and editing, Q.Z.; visualization, Q.Z.; supervision, Q.Z.; project administration, Q.Z.; funding acquisition, X.Z. All authors have read and agreed to the published version of the manuscript.

Funding: This study was funded by the National Natural Science Foundation of China (52078143).

Institutional Review Board Statement: Not applicable.

Informed Consent Statement: Informed consent was obtained from all subjects involved in the study. Written informed consent has been obtained from the patient(s) to publish this paper.

Data Availability Statement: The data that support the findings of this study are available from the corresponding author upon reasonable request.

Conflicts of Interest: The authors declare no conflict of interest.

References

- Meng, Y.X. Research on the forms of advanced support reinforcement for tunnels in weak surrounding rocks. *J. Munic. Technol.* **2023**, *41*, 111–116.
- Liu, R. Prediction of surface deformation during construction of railway tunnels crossing karst areas. *J. Munic. Technol.* **2023**, *41*, 129–136.
- Liu, J. Study on safety of support structure in karst section of tunnel considering fluid-solid coupling. *J. Munic. Technol.* **2023**, *41*, 84–90.
- Li, S.C.; Xu, Z.H.; Huang, X.; Lin, P.; Zhao, X.C.; Zhang, Q.S.; Yang, L.; Zhang, X.; Sun, H.F.; Pan, D.D. Classification, geological identification, hazard mode and typical case studies of hazard-causing structures for water and mud inrush in tunnels. *Chin. J. Rock Mech. Eng.* **2018**, *37*, 1043–1069.
- Golian, M.; Teshnizi, E.S.; Nakhaei, M. Prediction of water inflow to mechanized tunnels during tunnel-boring-machine advance using numerical simulation. *Hydrogeol. J.* **2018**, *26*, 2827–2851. [[CrossRef](#)]
- Liu, J.; Chen, W.; Yuan, J.; Li, C.; Zhang, Q.; Li, X. Groundwater control and curtain grouting for tunnel construction in completely weathered granite. *Bull. Eng. Geol. Environ.* **2018**, *77*, 515–531. [[CrossRef](#)]
- Liu, J.-Q.; Yuen, K.-V.; Chen, W.-Z.; Zhou, X.-S.; Wang, W. Grouting for water and mud inrush control in weathered granite tunnel: A case study. *Eng. Geol.* **2020**, *279*, 105896. [[CrossRef](#)]
- Li, S.C.; Wang, K.; Li, L.P.; Zhang, Q.S.; Hu, C.; Zhou, Y.; Liu, H.L.; Lin, P. Development and application of an extendable model test system for water inrush simulation in subsea tunnel. *Chin. J. Rock Mech. Eng.* **2014**, *33*, 2409–2418.
- Li, W.P.; Liu, Q.M.; Sun, R.H. Theoretical and experiment study on vadose conversion of water inrush later occurred from structure broken zone. *Coal Sci. Technol.* **2011**, *39*, 10–13.
- Zhang, Q.S.; Wang, D.M.; Li, S.C.; Zhang, X.; Tan, Y.H.; Wang, K. Development and application of model test system for inrush of water and mud of tunnel in fault rupture zone. *Chin. J. Geotech. Eng.* **2017**, *39*, 417–426.
- Xiexing, M.; Zhanqing, C.; Xianbiao, M.; Ronghua, C. The bifurcation of non-Darcy flow in post-failure rock. *Acta Mech. Sin.* **2003**, *35*, 660–667.
- Li, S.C.; Miao, X.X.; Chen, Z.Q. Non-linear dynamic analysis on non-Darcy seepage in over-broken rock mass. *J. China Coal Soc.* **2005**, *30*, 557–561.

13. Chen, Z.Q.; Wang, L.Z.; Kong, H.L.; Yao, B.H. Study on non-linear seepage test of variable mass of broken rock. *Saf. Coal Mines* **2014**, *45*, 15–21.
14. Wang, J.A.; Park, H.D. Coal mining above a confined aquifer. *Int. J. Rock Mech. Min.* **2003**, *40*, 537–551. [[CrossRef](#)]
15. Font-Capó, J.; Vázquez-Suñé, E.; Carrera, J.; Martí, D.; Carbonell, R.; Pérez-Estaun, A. Groundwater inflow prediction in urban tunneling with a tunnel boring machine (TBM). *Eng. Geol.* **2011**, *121*, 46–54. [[CrossRef](#)]
16. Zhang, X.S.; Wong, H.; Leo, C.J.; Bui, T.A.; Wang, J.X.; Sun, W.H.; Huang, Z.Q. A Thermodynamics-Based Model on the Internal Erosion of Earth Structures. *Geotech. Geol. Eng.* **2013**, *31*, 479–492. [[CrossRef](#)]
17. Bonelli, S.; Marot, D. Micromechanical modeling of internal erosion. *J. Environ. Civ. Eng.* **2011**, *15*, 1207–1224. [[CrossRef](#)]
18. Fell, R.; Wan, C.F.; Cyganiewicz, J.; Foster, M. Time for Development of Internal Erosion and Piping in Embankment Dams. *J. Geotech. Geoenviron. Eng.* **2003**, *129*, 307–314. [[CrossRef](#)]
19. Yerro, A.; Rohe, A.; Soga, K. Modelling Internal Erosion with the Material Point Method. *Procedia Eng.* **2017**, *175*, 365–372. [[CrossRef](#)]
20. Rönnqvist, H.; Fannin, J.; Viklander, P. On the use of empirical methods for assessment of filters in embankment dams. *Geotech. Lett.* **2014**, *4*, 272–282. [[CrossRef](#)]
21. Liu, J.; Chen, W.; Nie, W.; Yuan, J.; Dong, J. Experimental research on the mass transfer and flow properties of water inrush in completely weathered granite under different particle size distributions. *Rock Mech. Rock Eng.* **2019**, *52*, 2141–2153. [[CrossRef](#)]
22. Liu, J.; Zhou, C. Permeability-porosity relation during erosion-induced water inrush: Experimental and theoretical investigations. *Transp. Geotech.* **2023**, *38*, 100893. [[CrossRef](#)]
23. Kong, F.; Xue, Y.; Gong, H.; Jiang, X.; Song, Q.; Fu, Y.; Fu, K. The formation mechanism of dynamic water and mud inrush geohazard triggered by deep-buried tunnel crossing active fault: Insights from the geomechanical model test. *Tunn. Undergr. Space Technol.* **2023**, *142*, 105437. [[CrossRef](#)]
24. Li, S.C.; Wu, J.; Xu, Z.H.; Li, L.P. Unascertained measure model of water and mud inrush risk evaluation in karst tunnels and its engineering application. *KSCE J. Civ. Eng.* **2016**, *21*, 1170–1182. [[CrossRef](#)]
25. Sterpi, D. Effects of the Erosion and Transport of Fine Particles due to Seepage Flow. *Int. J. Géoméch.* **2003**, *3*, 111–122. [[CrossRef](#)]
26. Cividini, A.; Gioda, G. Finite-Element Approach to the Erosion and Transport of Fine Particles in Granular Soils. *Int. J. Géoméch.* **2004**, *4*, 191–198. [[CrossRef](#)]
27. Papamichos, E.; Vardoulakis, I. Sand erosion with a porosity diffusion law. *Comput. Geotech.* **2005**, *32*, 47–58. [[CrossRef](#)]
28. Bear, J. *Dynamics of Fluids in Porous Media*; American Elsevier: New York, NY, USA, 1972.
29. Li, T.; Mei, T.; Sun, X.; Lv, Y.; Sheng, J.; Cai, M. A study on a water-inrush incident at Laohutai coalmine. *Int. J. Rock Mech. Min. Sci.* **2013**, *59*, 151–159. [[CrossRef](#)]
30. Yang, T.; Chen, S.; Zhu, W.; Meng, Z.; Gao, Y. Water inrush mechanism in mines and nonlinear flow model for fractured rocks. *Chin. J. Rock Mech. Eng.* **2008**, *27*, 1411–1416.
31. Xue, Y.-Q. *Principle of Groundwater Dynamics*; Geological Publishing House: Beijing, China, 1986.
32. Brinkman, H.C. A calculation of the viscous force exerted by a flowing fluid on a dense swarm of particles. *Appl. Sci. Res.* **1949**, *1*, 27–34. [[CrossRef](#)]
33. Hill, A.A.; Carr, M. Nonlinear stability of the one-domain approach to modelling convection in superposed fluid and porous layers. *Proc. R. Soc. A. Math. Phys. Eng. Sci.* **2010**, *466*, 2695–2705. [[CrossRef](#)]
34. Rahmati, H.; Jafarpour, M.; Azadbakht, S.; Nouri, A.; Vaziri, H.; Chan, D.; Xiao, Y. Review of sand production prediction models. *J. Pet. Eng.* **2013**, *2013*, 864981. [[CrossRef](#)]
35. Vardoulakis, I.; Stavropoulou, M.; Papanastasiou, P. Hydromechanical aspects of the sand production problem. *Transp. Porous Med.* **1996**, *22*, 225–244. [[CrossRef](#)]
36. Zhang, Q.Y.; Chen, W.Z.; Yuan, J.Q.; Liu, L.Q.; Rong, C. Experimental study on evolution characteristics of water and mud inrush in fault fractured zone. *Rock Soil Mech.* **2020**, *41*, 1911–1922.
37. Wang, D.-M.; Zhang, Q.-S.; Zhang, X.; Wang, K.; Tan, Y.-H. Model experiment on inrush of water and mud and catastrophic evolution in a fault fracture zone tunnel. *Rock Soil Mech.* **2016**, *37*, 2851–2860.
38. Tan, Y. Evolutionary Mechanism of Mud Bursting through Water-Inrich Fault in Tunnels and Engineering Applications. Master's Thesis, Shandong University, Jinan, China, 2017.

Disclaimer/Publisher's Note: The statements, opinions and data contained in all publications are solely those of the individual author(s) and contributor(s) and not of MDPI and/or the editor(s). MDPI and/or the editor(s) disclaim responsibility for any injury to people or property resulting from any ideas, methods, instructions or products referred to in the content.